

An_{1.33}T₄Al₈Si₂ (An = Ce, Th, U, Np; T = Ni, Co): Actinide Intermetallics with Disordered Gd_{1+x}Fe₄Si_{10-y} Structure Type Grown from Metal Flux

Ashini S. Jayasinghe, You Lai, Wesley M. Potter, Cory J. Windorff, Ryan Baumbach, Thomas E. Albrecht-Schönzart, and Susan E. Lattner*

Cite This: *Inorg. Chem.* 2021, 60, 13062–13070

Read Online

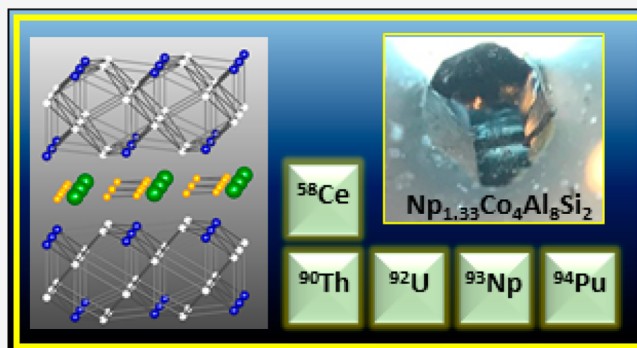
ACCESS |

Metrics & More

Article Recommendations

Supporting Information

ABSTRACT: An_{1.33}T₄Al₈Si₂ (An = Ce, Th, U, Np; T = Ni, Co) were synthesized in metal flux reactions carried out in aluminum/gallium melts. In previous work, U_{1.33}T₄Al₈Si₂ (T = Co, Ni) analogues were formed by arc-melting U:T:Si and reacting this mixture in Al/Ga flux. However, in the current work, all compounds were synthesized by using AnO₂ reactants, taking advantage of the ability of the aluminum in the flux to act as both solvent and reducing agent. While reactions with T = Co yielded hexagonal Gd_{1.33}Fe₄Si_{10-y}-type quaternary phases for all An, reactions with T = Ni produced these compounds only with An = U and Np. For reactions with An = Ce and Th, the reactions led instead to the formation of AnNi_{3-x}Si_xAl_{4-y}Ga_y phases, with the tetragonal KCu₃S₄ structure type. Attempts to synthesize plutonium analogues Pu_{1.33}T₄Al₈Si₂ were also unsuccessful, producing the previously reported PuCoGa₅ and Pu₂Ni₅Si₆ instead. Magnetic data collected on the neptunium analogues Np_{1.33}T₄Al₈Si₂ (T = Ni, Co) show antiferromagnetic coupling at low temperatures and indicate a tetravalent state for the Np ions.



INTRODUCTION

Nuclear reactors provide 20% of the US's energy requirement and act as a greener approach to produce electricity compared to most other existing energy-generating methods.^{1–3} The nuclear fuel rods in reactors contain uranium dioxide pellets that are stacked and sealed inside metal rods. After five years, these nuclear rods are replaced. At this point, spent nuclear fuel rods are still highly radioactive and are thus stored underwater in steel-lined concrete pools for at least one year, allowing the fuel to cool and radioactivity to decrease. Afterward, spent fuel rods are transferred to stainless steel canisters and welded or bolted shut, and then these are placed in concrete containers. These storage systems are known as dry casks, and there are varying designs. As there is no permanent storage repository in the US, the spent nuclear fuel is sitting in dry casks at or near power plants.^{4–7} Environmental factors such as humidity, inclement weather, and potential flooding have adverse effects on these stainless steel casks. When preparing these hazardous contents for long-term storage, scientists are predicting previously unforeseen obstacles such as accelerated corrosion at the interface of different barrier materials.^{8–11} Thus, proceeding with long-term storage for nuclear waste requires an in-depth understanding of actinide oxides and their interactions with metals.

Relative to transition metals and lanthanides, research on actinides has been limited; this is particularly true for transuranic compounds due to their scarcity and level of radioactivity. Despite this difficulty, transuranic materials have gained interest due to reports of intriguing chemical and physical properties such as superconductivity, spin glass phenomena, and heavy fermion behavior.^{12–14} As an example, NpNiSi₂ displays heavy fermion behavior with a Sommerfeld coefficient of 133 mJ mol⁻¹ K⁻² and exhibits reduced magnetic moment due to the Kondo effect.^{15,16} Also, PuCoGa₅, PuRhGa₅, PuCoIn₅, and PuRhIn₅ are plutonium-based superconductors in the “115” family. It is presumed their 5f electrons are inducing most of these unique characteristics.^{17–24}

Metal flux growth has proven to be a successful method for the synthesis of transuranic intermetallic materials.^{16,17,23,25} The other techniques that are commonly used to generate

Received: May 17, 2021

Published: August 17, 2021

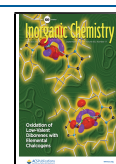


Table 1. Products Obtained from $\text{AnO}_2/(\text{Ni or Co})/\text{Si}/\text{Al}/\text{Ga}$ Reactions^a

reactants	millimole ratio	products
CeO ₂ :Ni:Si:Al:Ga	0.5:1:1:10:10	CeNi _{2.32} Al ₄ Si _{0.68} (60%)
CeO ₂ :Co:Si:Al:Ga	0.5:1:1:10:10	Ce _{1.33} Co ₄ Al ₈ Si ₂ (20%), <i>unknown quaternary monoclinic phase</i> (45%)
UO ₂ :Ni:Si:Al:Ga	0.5:1:1:10:10	U _{1.33} Ni ₄ Al ₈ Si ₂ (50%), U(Al/Si/Ga) ₃ (15%)
UO ₂ :Co:Si:Al:Ga	0.5:1:1:10:10	U _{1.33} Co ₄ Al ₈ Si ₂ (70%)
ThO ₂ :Ni:Si:Al:Ga	0.5:1:1:10:10	ThNi _{2.04} Al ₄ Si _{0.96} (65%)
ThO ₂ :Ni:Si:Al:Ga	0.037:0.074:0.074:0.741:0.741	ThNi _{2.04} Al ₄ Si _{0.96} (50%), Th _{1.33} Ni ₄ Al ₈ Si ₂ (5%)
ThO ₂ :Co:Si:Al:Ga	0.5:1:1:10:10	Th _{1.33} Co ₄ Al ₈ Si ₂ (50%)
NpO ₂ :Ni:Si:Al:Ga	0.037:0.074:0.074:0.741:0.741	Np _{1.33} Ni ₄ Al ₈ Si ₂ (30%), Np(Al/Si/Ga) ₃ (10%)
NpO ₂ :Co:Si:Al:Ga	0.037:0.074:0.074:0.741:0.741	Np _{1.33} Co ₄ Al ₈ Si ₂ (25%)
PuO ₂ :Ni:Si:Al:Ga	0.037:0.074:0.074:0.741:0.741	Pu ₂ Ni ₃ Si ₅ (40%)
PuO ₂ :Co:Si:Al:Ga	0.037:0.074:0.074:0.741:0.741	PuCoGa ₅ (10%)

^aThe italicized products are different from the primary hexagonal Gd_{1.33}Fe₄Si₁₀-type phase. The yields (based on AnO₂ reactant) are reported next to each product.

intermetallics are arc-melting or traditional solid-state synthesis.^{26–29} However, these methods require that actinide reactants be in their metallic elemental form. In flux growth reactions, if a strong reducing flux such as aluminum is used, then metal oxides can be used as a reagent. The solution state of flux reactions is also advantageous, dissolving the radioactive reactants in excess of molten metal; this avoids the hazards of arc-melting transuranic materials (which may involve volatilizing or sputtering radioactive materials in the apparatus). So flux chemistry provides a safe and convenient platform to create novel complex actinide intermetallic materials.³⁰

In previous work, two quaternary uranium intermetallic materials were synthesized by using Al/Ga flux. U_{1.33}T₄Al₈Si₂ (T = Ni, Co) formed in the hexagonal Gd_{1+x}Fe₄Si_{10–y} structure type which exhibits a characteristic structural disorder in the uranium atom arrangement that leads to interesting magnetic phenomena such as fragile magnetic ordering and spin-glass-like behavior.³¹ In the current work, these studies were expanded to explore Ce, Th, and Np analogues of these phases. Having a series of materials provides an opportunity not only to compare the effect of varying the rare-earth but also to analyze the impact of transition metal on its properties. Five new analogues of An_{1.33}T₄Al₈Si₂ (An = Ce, Th, Np; T = Ni, Co) were formed. Magnetic data collected on the neptunium analogues show antiferromagnetic coupling at low temperatures and indicate a tetravalent state for the Np ions. Attempts to synthesize plutonium analogues led instead to the growth of PuCoGa₅ and Pu₂Ni₃Si₅. Reactions targeting An_{1.33}Ni₄Al₈Si₂ with An = Th and Ce led to the formation of AnNi_{3–x}Si_xAl_{4–y}Ga_y with the tetragonal KCu₄S₃ structure type.

EXPERIMENTAL PROCEDURE

Synthesis. *Caution:* UO₂, ThO₂, NpO₂, and PuO₂ used in the reactions contain radioactive isotopes²³⁸U, ²³²Th, ²³⁷Np, and ²³⁹Pu which are α -emitters and like all radioactive materials must be handled with care. These experiments were conducted by trained personnel in a licensed research facility with special precautions taken toward the handling, monitoring, and disposal of radioactive materials.

In the previous work, U_{1.33}T₄Al₈Si₂ (T = Co, Ni) were synthesized by arc-melting uranium pieces, transition metal slugs, and silicon wafer pieces in a 0.5:1:1 U/T/Si mmol ratio. The arc-melted mixture was placed in an alumina crucible and was reacted with 10 mmol of aluminum and 10 mmol of gallium to form the products.³¹ However, Np and Pu metals are difficult to obtain, and arc-melting them has the potential to be hazardous; thus, the synthesis method was modified to use AnO₂ instead. For comparison, attempts were made to synthesize U_{1.33}T₄Al₈Si₂ materials by using UO₂ instead of uranium metal. Before

using UO₂ in the reaction, we baked it at 650 °C to remove any absorbed water. Once reactions with UO₂ were confirmed to be successful, reactions with thorium dioxide and cerium dioxide were conducted. For these reactions, 0.5 mmol of AnO₂ (An = U, Th, or Ce) was reacted with 1 mmol of Ni or Co and 1 mmol of Si in 10 mmol of Al and 10 mmol of Ga flux.

To conduct Np or Pu reactions, the reactants had to be scaled down due to their higher radioactivity. Scaled-down reactions were first executed with uranium and thorium dioxide as the actinide by using 10 mg of actinide oxides and scaling down the other reaction components accordingly (vide infra). After confirming the scaled-down reactions can be conducted successfully, we made attempts to synthesize Np and Pu analogues with Ni and Co as the transition metal. The actinide dioxide weight was set to 10 mg, and the quantities of the other elements were calculated to achieve the An:T:Si:Al:Ga molar ratio of 0.5:1:1:10:10. These were placed in small 0.5 mL alumina crucibles instead of the standard scale 2.0 mL crucibles. The crucibles were placed in quartz sleeves along with silica wool on top to act as a filter. The tubes were sealed under vacuum, then heated to 1000 °C in 12 h and maintained at that temperature for 48 h, and then cooled to 800 °C in 72 h. The reaction ampules were taken out of the furnace and centrifuged to separate excess flux from the product crystals.

Elemental Analysis. Semiquantitative elemental analysis data were obtained by using an FEI NOVA 400 scanning electron microscope (SEM) coupled with energy-dispersive X-ray spectroscopy (EDS). Selected crystals were cleaved to expose their interior regions to eliminate erroneous analyses due to flux residue that can adhere to the outside of the crystals. Sample surfaces were oriented on carbon tape perpendicular to the electron beam. The crystals were analyzed by using a 30 kV accelerating voltage. The SEM/EDS data are reported in the Supporting Information (Tables S11–S14).

Structural Analysis. Smaller pieces cleaved from single crystals were coated in oil, placed in MiTeGen holders, and mounted on a Bruker D8 Quest single-crystal X-ray diffractometer equipped with Mo K α radiation ($\lambda = 0.7107$ Å). Data were collected at room temperature, and peak intensities were corrected for Lorentz, polarization, and background effects by using the Bruker APEX III software.^{32,33} An empirical absorption correction was applied by using the program SADABS, and the structure solution was determined by intrinsic phasing methods and refined on the basis of F2 for all unique data using the SHELXTL program suite.³⁴ Aluminum and silicon are indistinguishable in X-ray diffraction experiments, so light element sites in the structure were assigned as either Al or Si based on bond lengths to neighboring atoms and consideration of the Al/Si ratios observed in the elemental analysis of samples (see the Discussion section). X-ray diffraction precession images of *h*0*l* and *h*k0 zones were collected on An_{1.33}T₄Al₈Si₂ crystals with 100 s exposure time. Crystallographic data for phases listed in Table 1 are available as CIF files from the Cambridge Crystallographic Data Centre under deposition numbers 2082974–2082982. Selected bond lengths and

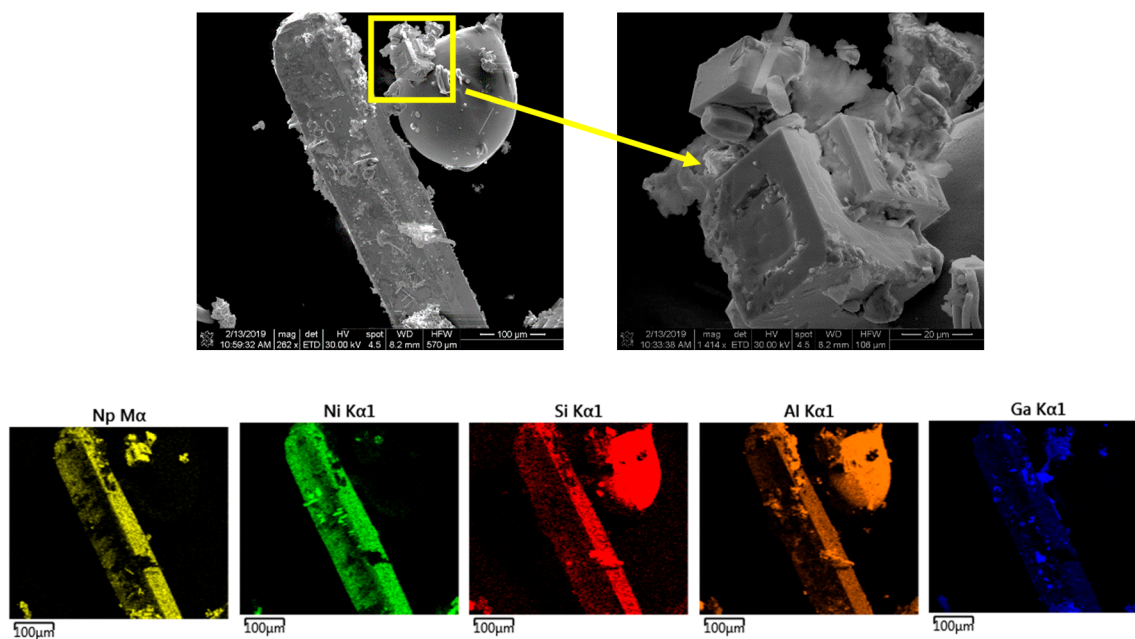


Figure 1. SEM/EDS images of rod-shaped $\text{Np}_{1.33}\text{Ni}_4\text{Al}_8\text{Si}_2$ crystals and cubic $\text{Np}(\text{Al}/\text{Si}/\text{Ga})_3$ phase, with the compounds clearly distinguishable by different crystal habit and confirmed by element mapping. Spherical Al/Si-rich structure is a silicate fragment from the Fiberfrax.

crystallographic data are provided in Supporting Information (Tables S15–S113).

Magnetic Susceptibility Measurements. Measurements of the magnetization were performed on oriented crystals of selected $\text{An}_{1.33}\text{T}_4\text{Al}_8\text{Si}_2$ phases using a Quantum Design MPMS3 magnetometer. The temperature-dependent DC magnetic susceptibility data $\chi = M/H$ were measured between $T = 1.8$ and 300 K by using applied fields $H = 100$ and 1000 Oe; field-dependent magnetization data $M(H)$ were collected at $T = 1.8$ K for $H < 7$ T.

RESULTS AND DISCUSSION

Synthesis. The products obtained in $\text{AnO}_2/(\text{Ni or Co})/\text{Si}/\text{Al}/\text{Ga}$ reactions are summarized in Table 1. When syntheses were conducted with oxides CeO_2 , ThO_2 , UO_2 , and NpO_2 and cobalt as the transition metal, pencil-shaped (faceted rods with hexagonal cross section and pointed ends) $\text{An}_{1.33}\text{Co}_4\text{Al}_8\text{Si}_2$ crystals were formed, with no byproducts observed (Figures S11 and S12). However, reactions with nickel as the transition metal were far less consistent. When Ni was used as the transition metal with uranium dioxide, $\text{U}_{1.33}\text{Ni}_4\text{Al}_8\text{Si}_2$ is formed, but a byproduct is also observed (cubic $\text{U}(\text{Al}/\text{Si}/\text{Ga})_3$ with the Cu_3Au structure type). Reactions with NpO_2 and nickel yield similar results ($\text{Np}_{1.33}\text{Ni}_4\text{Al}_8\text{Si}_2$ and byproduct $\text{Np}(\text{Al}/\text{Si}/\text{Ga})_3$). As can be seen from Figure 1, the two phases can be distinguished easily due to their distinct crystal habits. With CeO_2 and ThO_2 , the $\text{An}_{1.33}\text{Ni}_4\text{Al}_8\text{Si}_2$ phase was not formed at all; instead, plate-shaped crystals of tetragonal phase $\text{AnNi}_{3-x}\text{Si}_x\text{Al}_{4-y}\text{Ga}_y$ formed. However, scaling down the ThO_2 reaction (using 10 mg of ThO_2) led to the formation of the $\text{Th}_{1.33}\text{Ni}_4\text{Al}_8\text{Si}_2$ phase as a byproduct.

Efforts to form $\text{Pu}_{1.33}\text{T}_4\text{Al}_8\text{Si}_2$ were unsuccessful. Reactions with transition metals Co and Ni produced plate-shaped PuCoGa_5 and blocky $\text{Pu}_2\text{Ni}_3\text{Si}_5$ crystals (Figure S13), respectively. These materials have been previously reported and well characterized. PuCoGa_5 (tetragonal CeCoIn_5 type, Figure S14) is a known unconventional superconductor.^{18,19} $\text{Pu}_2\text{Ni}_3\text{Si}_5$ (orthorhombic $\text{U}_2\text{Co}_3\text{Si}_5$ type, Figure S15) contains one crystallographically unique Pu site, two Ni sites, and three

Si sites. Single-crystal data on our samples indicate that one of the Si sites includes another element with a higher atomic weight than Si, which can be either Ga or Ni. SEM/EDS data indicated Ga incorporation. The mixed site refinement as a Si/Ga mixture leads to a 78% Si/22% Ga ratio and an overall stoichiometry $\text{Pu}_2\text{Ni}_3\text{Ga}_{0.44}\text{Si}_{4.56}$, which agrees well with the SEM/EDS data (Table S12). Bauer et al. reported the synthesis of $\text{Pu}_2\text{Ni}_3\text{Si}_5$ in Ga flux. In that structure, Ni mixes on the Si site; however, in the compound grown from Al/Ga flux, it appears that Ga is incorporated on this site instead.²⁵ The previous reports on PuCoGa_5 and $\text{Pu}_2\text{Ni}_3\text{Si}_5$ phases used Pu metal in their syntheses. The current work confirms that the use of mixed metal fluxes with a reducing metal such as Al presents the opportunity to use metal oxides to synthesize intermetallic materials instead of using elemental metals. As the metal oxide is reduced, it is assumed that aluminum oxide is formed in small quantities.

SEM-EDS data were collected on these materials to identify the elements which are present in the crystals. It is notable that SEM-EDS data are semiquantitative, and surface contamination (e.g., flux on the surface) can lead the results to be less accurate. While Al/Ga flux that is adhered to the surface can be cleaned by sonicating in a warm ethanol solution, this process is challenging for highly radioactive transuranic materials and was therefore not carried out. Another step that is usually implemented to negate the impact from surface contamination is cleaving the crystal to expose an interior surface and aligning this perpendicular to the electron beam. Again, this becomes more challenging for transuranic materials. The impact of surface flux is quite evident in SEM data. The Ga quantity detected in two neptunium compounds is higher than that for other materials, and based on the comparison with the theoretical atomic percentages, it can be concluded that this is due to surface contamination.

Structure. $\text{An}_{1.33}\text{T}_4\text{Al}_8\text{Si}_2$ phases form with the $\text{Gd}_{1+x}\text{Fe}_4\text{Si}_{10-y}$ structure type in the hexagonal $P6_3/mmc$ space group, as described in our previous work on the uranium

analogues.³¹ There is one crystallographically unique rare-earth site, one transition metal site, two aluminum sites, and one silicon site. The structure contains two main building blocks as shown in Figure 2. The first unit is the TAl_2 corrugated double

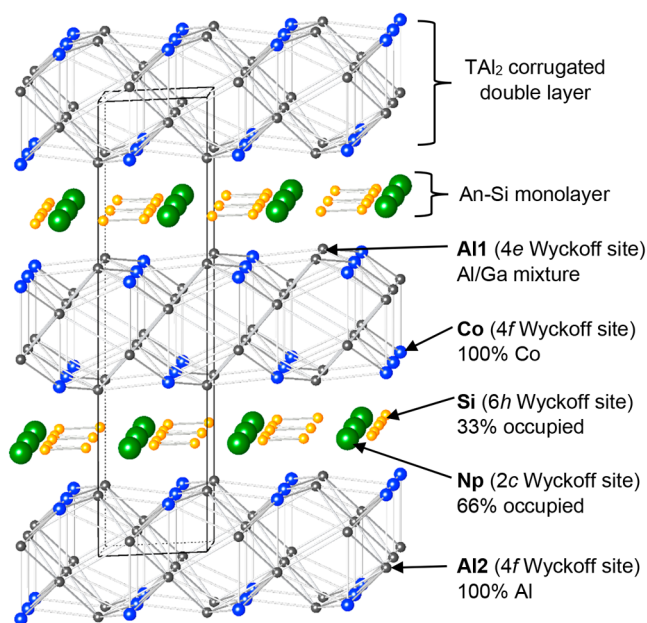


Figure 2. Structure of $\text{Np}_{1.33}\text{Co}_4\text{Al}_8\text{Si}_2$ viewed along a -axis; for clarity, the bonds between the layers are not depicted. Np, Co, Si, and Al are depicted as green, blue, gold, and gray spheres.

layer which can be described as a stuffed arsenic-type moiety. In $\text{Np}_{1.33}\text{Co}_4\text{Al}_8\text{Si}_2$, the Co–Al distances in this layer range from 2.4198(4) to 2.6457(12) Å, and the Al–Al bond distances range from 2.7732(16) to 2.779(3) Å. When the Al sites were freely refined, only the Al1, 4e Wyckoff site (the Al site in the outer layer of the double layer) indicated higher than 100% occupancy, so it was modeled as a mixed Al/Ga site, incorporating a small amount of gallium from the flux. This behavior was also seen in the uranium analogue. The Al/Ga percentages from occupancy refinement of this site were 85/15%, and this indicates a lower overall atomic percentage of gallium in the compound (4%) compared to the EDS data which indicate 10(2)% of gallium presence (the latter value may be skewed by flux adhered to the surface). Also, the SEM data (Table S13) generally showed slightly higher Si percentages and lower Al content than is indicated by the atomic ratios in the $\text{An}_{1.33}\text{T}_4\text{Al}_8\text{Si}_2$ model derived by using bond distances. This indicates possible Si mixing into these two Al sites (leading to $\text{An}_{1.33}\text{T}_4\text{Al}_{8-x}\text{Si}_{2+x}$ stoichiometries); however, neutron diffraction studies are required to confirm this.

These TAl_2 blocks are separated by the disordered An–Si layers; although not shown in Figure 2 for clarity, An–Al1 and T–Si bonds are present between the layers. For the $\text{Np}_{1.33}\text{Co}_4\text{Al}_8\text{Si}_2$ compound, the Np–Al and Co–Si bond distances are 3.0122(13) and 2.280(2) Å, respectively. For comparison, the Np–Al bond distances in NpFe_4Al_8 range from 2.891 to 2.951 Å, and the Co–Si bond distance in CoSi_2 is 2.323 Å.^{35–38} The prominent disorder inherent in the $\text{Gd}_{1+x}\text{Fe}_4\text{Si}_{10-y}$ structure type is found in the An–Si layer of $\text{An}_{1.33}\text{T}_4\text{Al}_8\text{Si}_2$. When the An (2c Wyckoff site) and Si (6h Wyckoff site) sites are refined as completely occupied, that

results in unrealistically short An–Si bond distances (e.g., 1.501(5) Å in $\text{Np}_{1.33}\text{Co}_4\text{Al}_8\text{Si}_2$). However, when the site occupancies are allowed to freely refine, the An and Si sites show occupancies of around 66% and 33%, respectively. Based on these percentages, it can be speculated that these atoms arrange as every third An site replaced with a triangle of Si; if this occurs in an ordered manner, it will lead to a formation of a supercell with a more realistic Np–Si bond distance of 2.960(4) Å. This atom arrangement is displayed in Figure SI6. The precession photos obtained for these crystals demonstrated supercell peaks along the $hk0$ directions, indicative of the partial formation of an $a^* = \sqrt{3}a$ supercell ($a^* = 7.2$ Å). However, along $h0l$ instead of peaks, streaks appeared, indicating stacking disorder along the c -axis. The complexity of the structure has been extensively described in the previous work on $\text{U}_{1.33}\text{T}_4\text{Al}_8\text{Si}_2$.³¹

As $\text{An}_{1.33}\text{T}_4\text{Al}_8\text{Si}_2$ compounds contain both Al and Si, distinguishing these atoms based on single-crystal X-ray diffraction can be challenging due to their similar electron counts. To obtain a better understanding of the Al/Si site preference, attempts were made to synthesize the analogous $\text{Ce}_{1.33}\text{Co}_4\text{Al}_{10}$ and $\text{Ce}_{1.33}\text{Co}_4\text{Al}_8\text{Ge}_2$ compounds for comparison. However, instead of forming the desired phases, both reactions led to the formation of CoAl_3 with Ga doping. Therefore, assignments of Al and Si sites in $\text{An}_{1.33}\text{T}_4\text{Al}_8\text{Si}_2$ were done by taking into account observed bond distances.

Obtaining a range of structural analogues provides an opportunity to study the effect of element substitution on compound synthesis, structure, and properties. Going from Th to Np analogues, unit cell parameters should decrease as the ionic radius of the actinide metal decreases, and the bond lengths to it shrink accordingly. Shorter An–(Al or Si) bond lengths and resultant smaller unit cell parameters are seen going from the thorium phases to the uranium phases. However, the neptunium analogues exhibit very similar bond lengths and unit cells to those of the uranium compounds (see Figure 3 and Table S15). The lack of expected shrinking may indicate a change of the oxidation state of the actinide. In intermetallic materials, charge balancing is generally not required, so the exact oxidation state of each element cannot be easily predicted. Thorium is always tetravalent in intermetallics; uranium is typically +3 or +4 in intermetallics. If Th and U are +4 and neptunium is trivalent, that would explain the deviations observed in Figure 3. However, the oxidation state of uranium in the $\text{U}_{1.33}\text{T}_4\text{Al}_8\text{Si}_2$ analogues was not conclusively indicated by our previous magnetic susceptibility studies, and this is also the case for the Np analogues studied here (see next section).³¹ Further studies such as EXAFS are needed to determine the oxidation states of the actinide elements in these materials.

It is evident that using cobalt as the transition metal favors the formation of the $\text{An}_{1.33}\text{T}_4\text{Al}_8\text{Si}_2$ structure compared to reactions using nickel. $\text{An}_{1.33}\text{Co}_4\text{Al}_8\text{Si}_2$ analogues are obtained in high yield with An = Ce, Th, U, and Np. However, when nickel is used, the $\text{An}_{1.33}\text{Ni}_4\text{Al}_8\text{Si}_2$ phase could be obtained as the major product only with U and Np (see Table 1). $\text{Th}_{1.33}\text{Ni}_4\text{Al}_8\text{Si}_2$ only formed (as a minor byproduct) when the reaction was scaled down, and the cerium analogue $\text{Ce}_{1.33}\text{Ni}_4\text{Al}_8\text{Si}_2$ was not formed at all. Incorporation of cobalt also facilitates further supercell ordering. In the previous report, zone photos for $\text{U}_{1.33}\text{Co}_4\text{Al}_8\text{Si}_2$ displayed sharper supercell peaks and better ordering in the An–Si layer compared to the more diffuse zone photo for $\text{U}_{1.33}\text{Ni}_4\text{Al}_8\text{Si}_2$;

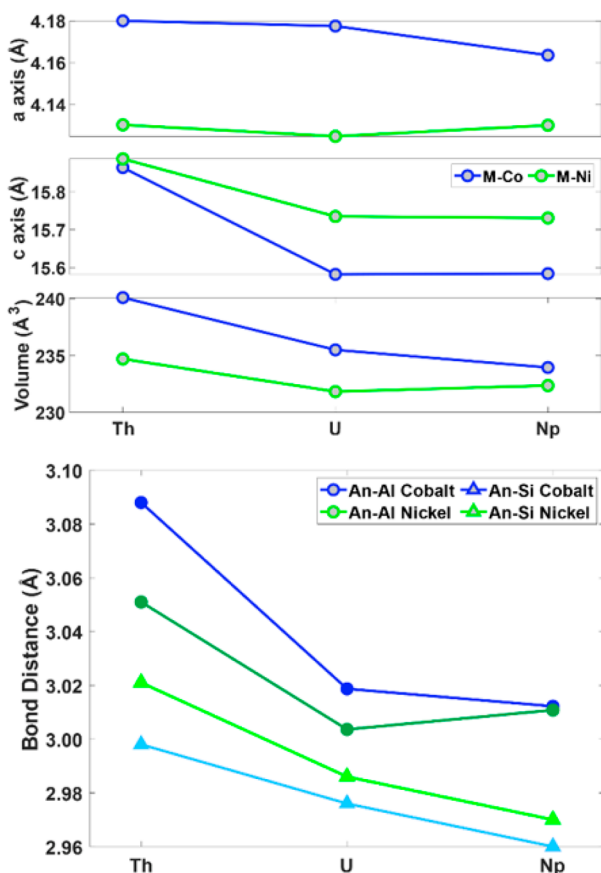


Figure 3. Unit cell lengths and selected bond distances of $An_{1.33}T_4Al_8Si_2$ crystals where An = Th, U, Np and T = Co (blue symbols), Ni (green symbols).

this data was supported by the U and Si percentages obtained in the refinement of single-crystal X-ray diffraction data.³¹ The current study also supports better ordering in cobalt analogues: in the thorium (Figure SI7) and neptunium compound zone photos, the Co analogue displayed a better-ordered structure relative to the Ni analogue (see Figure 4). In the SC-XRD data of the cobalt analogues, the refinements of sites in the An–Si layer show an actinide occupancy range from 65 to 70% and a silicon site range from 29 to 32%. These values are close to the ideal occupancies of 66 and 33% for An and Si sites in the supercell model. In the nickel compounds, the An site occupancy ranges from 52 to 56% and the Si site ranges from 34 to 43%. This data demonstrates the transition metals used in the reaction can impact the ordering of the structure. The exact reason for this is not known and it might be due to the varying ionic radius of the transition metal.

Reactions targeting $An_{1.33}Ni_4Al_8Si_2$ with An = Ce or Th instead yielded tetragonal phases $AnNi_{3-x}Si_xAl_{4-y}Ga_y$ ($CeNi_{2.32}Si_{0.68}Al_{3.67}Ga_{0.33}$ and $ThNi_{2.04}Si_{0.96}Al_{3.73}Ga_{0.27}$). It is notable that both structure types have similar An:Ni:Al:Si element ratios approaching 1:2:4:1, although the hexagonal title phase is poorer in An. The $AnNi_{3-x}Si_xAl_{4-y}Ga_y$ compounds have the KCu_4S_3 structure type which can be described as a combination of $BaAl_4$ -type layers with antifluorite-type $NiAl_2$ blocks (see Figure 5). This structure has also been reported for $EuAu_2Al_4Si$.³⁹ The $BaAl_4$ type layer is composed of the An cation (on the “barium” position) surrounded by eight symmetry-equivalent Ni/Si mixed sites. The An–An distance

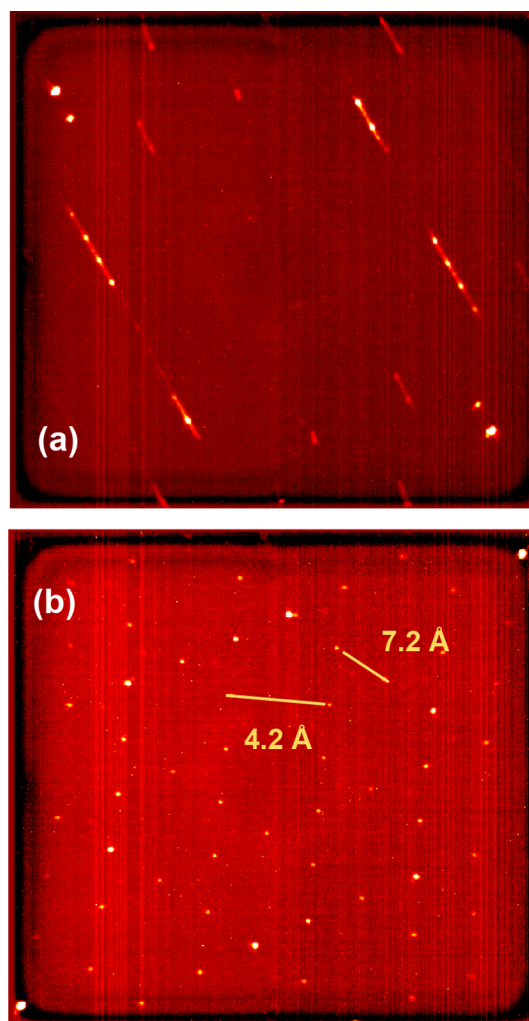


Figure 4. Zone photos collected on a crystal of $Np_{1.33}Co_4Al_8Si_2$: (a) Ok_l photo (down the a -axis) and (b) hk_0 photo (down the c -axis).

is identical with the a -axis unit cell parameter. The distance between Ni/Si sites to each other is 2.381(1) and 2.303(3) Å for Ce and Th analogues, respectively. The Ni/Si mixed site contains 66% Ni for the cerium analogue and 52% Ni for the thorium analogue, yielding respective stoichiometries of $CeNi_{2.33}Al_4Si_{0.67}$ and $ThNi_{2.04}Al_4Si_{0.96}$. The An–Ni/Si bond length is 3.1823(3) and 3.1296(6) Å for Ce and Th analogues, respectively. The Ce–Ni bond distance is slightly longer than the reported distances 2.956 and 2.821 Å for $CeNi$ and $CeNi_3$ compounds, respectively.^{40,41} In Ce_5Si_3 the Ce–Si bond distance is 2.920 Å, and in Ce_5Si_4 this bond distance ranges from 2.943 to 2.969 Å.^{42–46} The $CeNi_{2.33}Al_4Si_{0.67}$ compound displays longer bond distances compared to its Th analogue. In intermetallic compounds, thorium exclusively exhibits the tetravalent state, whereas Ce displays 3+ and 4+ oxidation states as well as mixed-valence states. So the longer bond distances in $CeNi_{2.33}Al_4Si_{0.67}$ might indicate that Ce is in the 3+ state. In Ce_5Si_3 and Ce_5Si_4 , Ce displays mixed valency, and in the latter, it is closer to the trivalent state.^{42–46} As indicated by the SEM/EDS data, another explanation for this discrepancy might be the higher Ga incorporation in the Ce analogue. As accurately refining a mixture of three elements on the same crystallographic site is nearly impossible, it is hard to predict the exact amount of Ga doping by using single-crystal

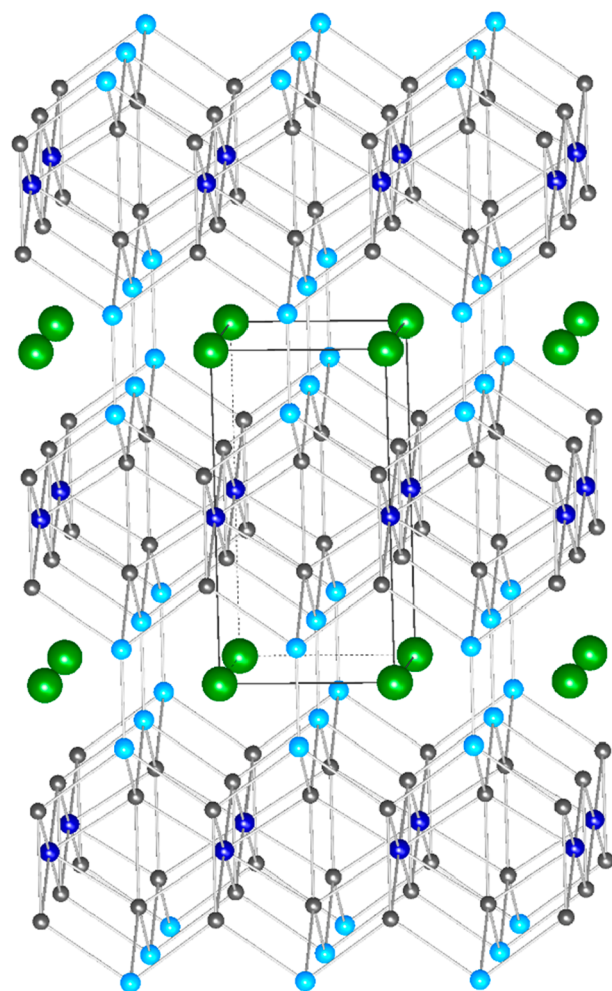


Figure 5. KCu_4S_3 -type tetragonal structure of $AnNi_{3-x}Si_xAl_{4-y}Ga_y$, viewed along the a -axis; for clarity, the bonds to the An ion are not depicted. An, Ni, Ni/Si, and Al are depicted as green, dark blue, light blue, and gray spheres, respectively.

X-ray diffraction. However, longer bond distances might indicate the incorporation of Ga into the Ni/Si sites.

In the antifluorite-type $NiAl_2$ slab, the Ni2 site is surrounded by eight crystallographically equivalent Al sites, and the Al is tetrahedrally coordinated to Ni atoms. The Al–Ni bond distance range is 2.4708(5)–2.5662(6) Å for $CeNi_{2.33}Al_4Si_{0.67}$ and 2.4496(8)–2.5114(11) Å for $ThNi_{2.04}Al_4Si_{0.96}$. The Al site occupancy refines slightly higher than unity, indicating slight incorporation of a heavier element (either Ga or Ni). SEM/EDS data shown in Table S14 support possible gallium incorporation, showing 6–17% of this element (with the caveat that the EDS measurement may be detecting flux coating). Refining the site as an Al/Ga mixture indicates 8–9% Ga incorporation, leading to stoichiometries of $CeNi_{2.32}Si_{0.68}Al_{3.67}Ga_{0.33}$ and $ThNi_{2.04}Si_{0.96}Al_{3.73}Ga_{0.27}$. SEM/EDS data also show 10.2 (± 0.4) and 18.5 (± 0.6) Si percentages in Ce and Th analogues; these are higher than the values observed by using single-crystal XRD, which were 8.5% and 12.0%, respectively. So it is possible excess Si could be mixing on the Al site. Refining this possible Al/Ga/Si mixture accurately using single-crystal X-ray diffraction is not possible.

Magnetic Behavior of $Np_{1.35}Co_4Al_{7.42}Ga_{0.58}Si_{1.73}$ and $Np_{1.12}Ni_4Al_{7.33}Ga_{0.67}Si_{2.55}$. Our previous work showed that

the combination of disorder, anisotropy, and the quasi-hexagonal planar arrangement of either trivalent or tetravalent uranium ions of the $U_{1.33}T_4Al_8Si_2$ compounds results in complex magnetic behavior, with nontrivial low-temperature ordered states.³¹ Similar behaviors are observed in the Np-based analogues. As seen in Figure 6, Curie–Weiss paramagnetism occurs at high temperatures. Fits to the data for 100 K $< T < 300$ K using the expression $\chi(T) = \chi_0 + C/T - \Theta$ yield $\chi_0 = -0.002$ and -0.004 cm³/mol, Weiss constants of $\Theta = -61$ and -31 K, and effective magnetic moments $\mu_{\text{eff}} \approx 3.5 \mu_B/\text{Np}$ for the Co and Ni variants, respectively. Assuming that the f-electron state is described by Hund's rules, the values for μ_{eff} are consistent with expectations for tetravalent Np ($\mu_{\text{eff}} = 3.62 \mu_B/\text{Np}$ for $[\text{Rn}]5f^2$). For comparison, we also show $\chi(T)$ for the Th–Co and Ce–Co analogues (Figure 6, right inset), which exhibit behavior that is consistent with Pauli paramagnetism in the absence of localized f-electron magnetism. This is the expected behavior for tetravalent thorium ($[\text{Rn}]4f^0$), where the magnetism is mainly due to the band electrons near the Fermi energy. Because similar behavior is observed for the cerium analogue, we infer that here the cerium electron configuration is also tetravalent, and indeed this suggests that throughout this family of materials tetravalency could be expected for the f-electron element. However, pinpointing the oxidation state of actinides from magnetic susceptibility data is difficult, as witnessed by the very similar magnetic moments for U^{3+} and U^{4+} (3.62 and 3.58 μ_B , respectively).⁴⁷ This is due to the effects of excited state mixing and intermediate coupling on the electronic states of these ions.^{48,49} It is also notable that the structural data in Figure 3 indicate a possible change in oxidation state going from uranium to neptunium. More studies are needed to conclusively determine the oxidation state of the actinides in these compounds.

Next, the negative Weiss temperatures for the Np compounds indicate that the magnetic exchange interaction is antiferromagnetic. We also note that these values are substantially smaller than those observed for the uranium-based analogues. Evidence for complex magnetic ordering is seen at low temperatures (Figure 6, left inset), where the Co version first shows a weak ferromagnetic-like increase near $T_{1,\text{Co}} = 46$ K and then an antiferromagnetic-like decrease near $T_{2,\text{Co}} = 6.5$ K. The Ni version also exhibits a strengthened increase in $\chi(T)$ that spans the temperature range near 10 K $< T < 50$ but is less well-defined. Subsequently, decreases at $T_{2,\text{Ni}} = 8$ K and $T_{3,\text{Ni}} = 3.9$ K are also observed. Taken together, these phenomena provide evidence for multiple magnetic ordering transitions resulting from neptunium f-states occurring in both $Np_{1.33}T_4Al_8Si_2$ analogues.

CONCLUSION

Reacting actinide oxide, transition metals ($T = \text{Ni}$ or Co), and Si in Al/Ga flux led to the formation of $An_{1.33}T_4Al_8Si_2$ quaternary phases with the hexagonal $Gd_{1.33}Fe_4Si_{10}$ type. When Co was used as the transition metal with $An = \text{Ce}, \text{Th}, \text{U},$ and Np , the expected $An_{1.33}T_4Al_8Si_2$ compounds were generated. However, reactions with Ni, with Ce and Th created tetragonal $AnNi_{3-x}Si_xAl_{4-y}Ga_y$ phases, with KCu_3S_4 structure type. The exact reason for this occurrence is not known; it is possibly due to the size of the transition metal as well as the larger radii of Th^{4+} and Ce^{3+} .

Having a series of isostructural materials provided the opportunity to compare the unit-cell parameters and bond

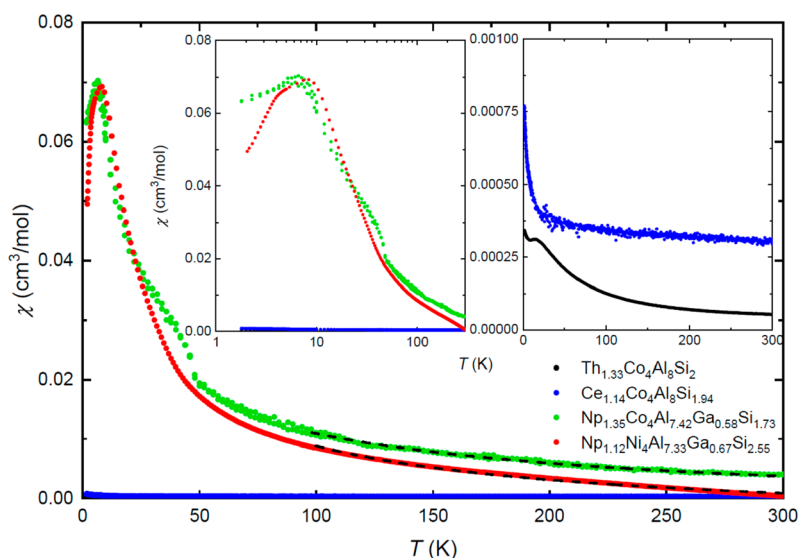


Figure 6. Magnetic susceptibility data for $\text{Np}_{1.35}\text{Co}_4\text{Al}_{7.42}\text{Ga}_{0.58}\text{Si}_{1.73}$, $\text{Np}_{1.12}\text{Ni}_4\text{Al}_{7.33}\text{Ga}_{0.67}\text{Si}_{2.55}$, and their Pauli paramagnetic Th- and Ce-based analogues for magnetic field $H = 5000$ Oe and temperatures $1.8 \text{ K} < T < 300 \text{ K}$. Left inset: same data presented on a linear-log scale to emphasize the region near magnetic ordering. Right inset: same data with the y -axis zoomed to emphasize the temperature dependences of the Th- and Ce-based specimens.

distances. It was expected that bond distances and unit cell parameters would decrease from Th to Np. For $\text{An}_{1.33}\text{Ni}_4\text{Al}_8\text{Si}_2$, the unit cell parameters do not follow the predicted pattern. For both compounds, the An–Al bond distance also deviates from the expected trend. A variation in oxidation states of the actinides present in these intermetallic materials might be giving rise to this divergence in pattern. It can be presumed thorium is in the $4+$ valence state. While magnetic susceptibility data suggest that U and Np are also tetravalent in these compounds, to unequivocally know the oxidation state of U and Np, EXAFS measurements are required. Attempts to make a Pu analogue to further the series were unsuccessful, leading instead to the formation of PuCoGa_5 and $\text{Pu}_2\text{Ni}_5\text{Si}_6$. These two compounds might be more thermodynamically stable than the hypothetical $\text{Pu}_{1.33}\text{T}_4\text{Al}_8\text{Si}_2$ phases; it is possible that varying the heating profiles to use lower temperatures or shorter dwell times might lead to the growth of the desired phase. Alternately, it may indicate that Pu^{4+} is too small to incorporate into the structure.

■ ASSOCIATED CONTENT

Supporting Information

The Supporting Information is available free of charge at <https://pubs.acs.org/doi/10.1021/acs.inorgchem.1c01480>.

Tables of elemental analysis data, crystallographic information, and bond lengths for $\text{An}_{1.33}\text{T}_4\text{Al}_8\text{Si}_2$ compounds and reaction byproducts; optical microscope and SEM images of flux-grown crystals; X-ray precession zone photos for $\text{An}_{1.33}\text{T}_4\text{Al}_8\text{Si}_2$ products; crystal structures of PuCoGa_5 and $\text{Pu}_2\text{Ni}_5\text{Si}_6$ (PDF)

Accession Codes

CCDC 2082974–2082982 contain the supplementary crystallographic data for this paper. These data can be obtained free of charge via www.ccdc.cam.ac.uk/data_request/cif, or by emailing data_request@ccdc.cam.ac.uk, or by contacting The Cambridge Crystallographic Data Centre, 12 Union Road, Cambridge CB2 1EZ, UK; fax: +44 1223 336033.

■ AUTHOR INFORMATION

Corresponding Author

Susan E. Latturmer – Department of Chemistry and Biochemistry, Florida State University, Tallahassee, Florida 32306, United States; orcid.org/0000-0002-6146-5333; Email: slatturmer@fsu.edu

Authors

Ashini S. Jayasinghe – Department of Chemistry and Biochemistry, Florida State University, Tallahassee, Florida 32306, United States

You Lai – Department of Physics, Florida State University and National High Magnetic Field Laboratory, Tallahassee, Florida 32310, United States

Wesley M. Potter – Department of Chemistry and Biochemistry, Florida State University, Tallahassee, Florida 32306, United States

Cory J. Windorff – Department of Chemistry and Biochemistry, Florida State University, Tallahassee, Florida 32306, United States

Ryan Baumbach – Department of Physics, Florida State University and National High Magnetic Field Laboratory, Tallahassee, Florida 32310, United States

Thomas E. Albrecht-Schönzart – Department of Chemistry and Biochemistry, Florida State University, Tallahassee, Florida 32306, United States

Complete contact information is available at: <https://pubs.acs.org/10.1021/acs.inorgchem.1c01480>

Notes

The authors declare no competing financial interest.

■ ACKNOWLEDGMENTS

This research was supported by the Center for Actinide Science and Technology (CAST), an Energy Frontier Research Center (EFRC) funded by the U.S. Department of Energy (DOE), Office of Science, Basic Energy Sciences (BES), under Award DE-SC0016568. Part of this work was

performed at the National High Magnetic Field Laboratory (NHMFL), which is supported by National Science Foundation Cooperative Agreements DMR-1157490 and DMR-1644779, the State of Florida, and the Department of Energy.

REFERENCES

- (1) Bowman, C.; Arthur, E.; Lisowski, P.; Lawrence, G.; Jensen, R.; Anderson, J.; Blind, B.; Cappiello, M.; Davidson, J.; England, T.; et al. Nuclear energy generation and waste transmutation using an accelerator-driven intense thermal neutron source. *Nucl. Instrum. Methods Phys. Res., Sect. A* **1992**, *320* (1–2), 336–367.
- (2) Schiermeier, Q.; Tollefson, J.; Scully, T.; Witze, A.; Morton, O. Energy alternatives: Electricity without carbon. *Nature* **2008**, *454* (7206), 816–823.
- (3) Worrall, A. Utilization of used nuclear fuel in a potential future US fuel cycle scenario. *WM2013*, Phoenix, AZ, 2013.
- (4) Bruno, J.; Ewing, R. C. Spent Nuclear Fuel. *Elements* **2006**, *2* (6), 343–349.
- (5) Ewing, R. C. Long-term storage of spent nuclear fuel. *Nat. Mater.* **2015**, *14* (3), 252–257.
- (6) Unger, S.; Krepper, E.; Beyer, M.; Hampel, U. Numerical optimization of a finned tube bundle heat exchanger arrangement for passive spent fuel pool cooling to ambient air. *Nucl. Eng. Des.* **2020**, *361*, 110549.
- (7) Ahearne, J. F. Prospects for nuclear energy. *Energy Econ.* **2011**, *33* (4), 572–580.
- (8) Goel, A.; McCloy, J. S.; Pokorny, R.; Kruger, A. A. Challenges with vitrification of Hanford High-Level Waste (HLW) to borosilicate glass—An overview. *J. Non-Cryst. Solids* **2019**, *4*, 100033.
- (9) Weirich, T. D.; Srinivasan, J.; Taylor, J. M.; Melia, M. A.; Noell, P. J.; Bryan, C. R.; Frankel, G. S.; Locke, J. S.; Schindelholz, E. J. Humidity effects on pitting of ground stainless steel exposed to sea salt particles. *J. Electrochem. Soc.* **2019**, *166* (11), C3477.
- (10) Guo, X.; Gin, S.; Lei, P.; Yao, T.; Liu, H.; Schreiber, D. K.; Ngo, D.; Viswanathan, G.; Li, T.; Kim, S. H.; et al. Self-accelerated corrosion of nuclear waste forms at material interfaces. *Nat. Mater.* **2020**, *19* (3), 310–316.
- (11) Zur Loye, H.-C.; Besmann, T.; Amoroso, J.; Brinkman, K.; Grandjean, A.; Henager, C. H.; Hu, S.; Mixture, S. T.; Phillpot, S. R.; Shustova, N. B.; Wang, H.; Koch, R. J.; Morrison, G.; Dolgoplova, E. Hierarchical Materials as Tailored Nuclear Waste Forms: A Perspective. *Chem. Mater.* **2018**, *30* (14), 4475–4488.
- (12) Sarrao, J. L.; Bauer, E. D.; Mitchell, J. N.; Tobash, P. H.; Thompson, J. D. Superconductivity in plutonium compounds. *Phys. C* **2015**, *514*, 184–188.
- (13) Aoki, D.; Haga, Y.; Matsuda, T. D.; Tateiwa, N.; Ikeda, S.; Homma, Y.; Sakai, H.; Shiokawa, Y.; Yamamoto, E.; Nakamura, A.; Settai, R.; Onuki, Y. Unconventional heavy-fermion superconductivity of a new transuranium compound NpPd₃Al₂. *J. Phys. Soc. Jpn.* **2007**, *76* (6), 063701.
- (14) Sarrao, J.; Morales, L.; Thompson, J. Superconductivity: A new window on plutonium's complexity. *JOM* **2003**, *55* (9), 38–40.
- (15) Thomas, C.; da Rosa Simoes, A. S.; Iglesias, J. R.; Lacroix, C.; Coqublin, B. Application of the underscreened Kondo lattice model to neptunium compounds. *J. Phys.: Conf. Ser.* **2012**, *391*, 012174.
- (16) Colineau, E.; Wastin, F.; Sanchez, J.; Rebizant, J. Magnetic properties of NpNiSi₂. *J. Phys.: Condens. Matter* **2008**, *20* (7), 075207.
- (17) Bauer, E. D.; Tobash, P. H.; Mitchell, J. N.; Sarrao, J. L. Single crystal growth of plutonium compounds from molten metal fluxes. *Philos. Mag.* **2012**, *92* (19–21), 2466–2491.
- (18) Thompson, J. D.; Curro, N. J.; Park, T.; Bauer, E. D.; Sarrao, J. L. PuCoGa₅ and related materials. *J. Alloys Compd.* **2007**, *444–445*, 19–22.
- (19) Curro, N.; Caldwell, T.; Bauer, E.; Morales, L.; Graf, M.; Bang, Y.; Balatsky, A.; Thompson, J.; Sarrao, J. Unconventional superconductivity in PuCoGa₅. *Nature* **2005**, *434* (7033), 622–625.
- (20) Opahle, I.; Oppeneer, P. M. Superconductivity Caused by the Pairing of Plutonium 5f Electrons in PuCoGa₅. *Phys. Rev. Lett.* **2003**, *90* (15), 157001.
- (21) Zhu, J.-X.; Tobash, P.; Bauer, E.; Ronning, F.; Scott, B.; Haule, K.; Kotliar, G.; Albers, R.; Wills, J. Electronic structure and correlation effects in PuCoIn₅ as compared to PuCoGa₅. *EPL* **2012**, *97* (5), 57001.
- (22) Bauer, E.; Altarawneh, M.; Tobash, P.; Gofryk, K.; Ayala-Valenzuela, O.; Mitchell, J.; McDonald, R.; Mielke, C.; Ronning, F.; Griveau, J.; et al. Localized 5f electrons in superconducting PuCoIn₅: consequences for superconductivity in PuCoGa₅. *J. Phys.: Condens. Matter* **2012**, *24* (5), 052206.
- (23) Haga, Y.; Aoki, D.; Matsuda, T. D.; Nakajima, K.; Arai, Y.; Yamamoto, E.; Nakamura, A.; Homma, Y.; Shiokawa, Y.; Onuki, Y. Single crystal growth and anisotropic superconducting property of PuRhGa₅. *J. Phys. Soc. Jpn.* **2005**, *74* (6), 1698–1701.
- (24) Bauer, E.; Tobash, P.; Mitchell, J.; Thompson, J. In *Probing the Nature of Superconductivity in the Heavy Fermion PuMGa₅ and PuMIn₅ (M= Co, Rh) Compounds*; APS March Meeting Abstracts, 2014; p G46.014.
- (25) Bauer, E.; Tobash, P.; Mitchell, J.; Kennison, J.; Ronning, F.; Scott, B.; Thompson, J. Magnetic order in Pu₂M₃Si₅ (M= Co, Ni). *J. Phys.: Condens. Matter* **2011**, *23* (9), 094223.
- (26) Wastin, F.; Rebizant, J.; Spirlet, J.; Sari, C.; Walker, C.; Fuger, J. New transuranium intermetallic compounds with ThCr₂Si₂ and CaBe₂Ge₂-type structures. *J. Alloys Compd.* **1993**, *196* (1–2), 87–92.
- (27) Meresse, Y.; Heathman, S.; Le Bihan, T.; Rebizant, J.; Brooks, M. S.; Ahuja, R. X-ray diffraction studies of AuCu₃-type neptunium compounds under pressure. *J. Alloys Compd.* **2000**, *296* (1–2), 27–32.
- (28) Wastin, F.; Rebizant, J.; Sanchez, J.; Blaise, A.; Goffart, J.; Spirlet, J.; Walker, C.; Fuger, J. New actinide ternary intermetallic compounds: synthesis, characterization and physical properties. *J. Alloys Compd.* **1994**, *210* (1–2), 83–89.
- (29) Wastin, F.; Rebizant, J.; Spirlet, J.; Fuger, J.; Kanellakopoulos, B.; Sechovsky, V. Magnetic study of new Pu(Mt: 3d, 4d or 5d transition metal)₂Si₂ intermetallic compounds. *J. Alloys Compd.* **1993**, *193* (1–2), 119–121.
- (30) Kanatzidis, M. G.; Pöttgen, R.; Jeitschko, W. The metal flux: a preparative tool for the exploration of intermetallic compounds. *Angew. Chem., Int. Ed.* **2005**, *44* (43), 6996–7023.
- (31) Jayasinghe, A. S.; Lai, Y.; Baumbach, R.; Lattner, S. E. U_{1.33}T₄Al₈Si₂ (T = Ni, Co): Complex Uranium Silicides Grown from Aluminum/Gallium Flux Mixtures. *Inorg. Chem.* **2019**, *58* (18), 12209–12217.
- (32) Sheldrick, G. *SHELXTLS*; Bruker-AXS: Madison, WI, 1998.
- (33) Hooft, R. *COLLECT*; Nonius BV: Delft, The Netherlands, 1996.
- (34) Sheldrick, G. M. A short history of SHELX. *Acta Crystallogr., Sect. A: Found. Crystallogr.* **2008**, *64* (1), 112–122.
- (35) Gonçalves, A.; Almeida, M.; Cardoso, C.; Gasche, T.; Godinho, M.; Boulet, P.; Colineau, E.; Wastin, F.; Rebizant, J. Magnetic properties of stoichiometric NpFe₄Al₈. *J. Phys.: Condens. Matter* **2005**, *17* (6), 909.
- (36) Gonçalves, A.; Almeida, M.; Wastin, F.; Colineau, E.; Boulet, P.; Javorský, P.; Rebizant, J. Electrical resistivity and specific heat studies of NpFe₄Al₈. *J. Alloys Compd.* **2006**, *416* (1–2), 164–168.
- (37) Maex, K. Silicides for integrated circuits: TiSi₂, CoSi₂. *Mater. Sci. Eng., R* **1993**, *11* (2–3), vii–153.
- (38) White, A. E.; Short, K.; Dynes, R.; Garno, J.; Gibson, J. Mesotaxy: Single-crystal growth of buried CoSi₂ layers. *Appl. Phys. Lett.* **1987**, *50* (2), 95–97.
- (39) Lattner, S. E.; Kanatzidis, M. G. RE(AuAl₂)_nAl₂(Au_xSi_{1-x})₂: A New Homologous Series of Quaternary Intermetallics Grown from Aluminum Flux. *Inorg. Chem.* **2008**, *47* (6), 2089–2097.
- (40) Finney, J. J.; Rosenzweig, A. The crystal structure of CeNi. *Acta Crystallogr.* **1961**, *14* (1), 69–69.

- (41) Sakurai, J.; Kamimura, H.; Ohyama, T.; Komura, Y.; Gignoux, D.; Lemaire, R. Thermopower of CeNi₅ and CeNi single crystals. *J. Magn. Magn. Mater.* **1987**, *70* (1–3), 383–384.
- (42) Kontani, M.; Senda, M.; Nakano, M.; Lawrence, J. M.; Adachi, K. Magnetic properties of Ce₅Si₃. *J. Magn. Magn. Mater.* **1987**, *70* (1–3), 378–380.
- (43) Nishioka, T.; Kobayashi, R.; Yasunami, T.; Kato, H.; Matsumura, M.; Kodama, K. Magnetic Properties of Ce₅Si₃ Single Crystal under Pressure. *J. Phys. Soc. Jpn.* **2007**, *76*, 45–46.
- (44) Ushida, Y.; Kontani, M. Magnetic phase diagram of Ce₅Si₃ single crystal. *Phys. B* **2000**, *281*, 86–87.
- (45) Sato, Y. J.; Shimizu, Y.; Nakamura, A.; Homma, Y.; Li, D.; Maurya, A.; Honda, F.; Aoki, D. Magnetic Properties of Heavy Fermion Compound Ce₅Si₄ with Chiral Structure. *J. Phys. Soc. Jpn.* **2018**, *87* (7), 074701.
- (46) Vejpravová, J.; Prokleška, J.; Daniš, S.; Sechovský, V. Antiferromagnetic ordering in Ce₅Si₄. *Phys. B* **2006**, *378*, 784–785.
- (47) Noguchi, S.; Okuda, K.; Abliz, M.; Goto, K.; Kindo, K.; Haga, Y.; Yamamoto, E.; Ōnuki, Y. High field magnetization of the new heavy fermion compound U_{1.2}Fe₄Si_{9.7}. *Phys. B* **1998**, *246–247*, 456–459.
- (48) Hendricks, M. E.; Jones, E. R.; Stone, J. A.; Karraker, D. G. Magnetic properties of trivalent actinides in the octahedral compounds Cs₂NaMCl₆. *J. Chem. Phys.* **1974**, *60*, 2095–2103.
- (49) Jung, J.; Atanasov, M.; Neese, F. Ab Initio ligand-field theory analysis and covalency trends in actinide and lanthanide free ions and octahedral complexes. *Inorg. Chem.* **2017**, *56*, 8802–8816.